Initial results and designs of dual-filter and plenoptic imaging for high-temperature plasmas

Zhen Sun, Jon K. Baldwin, Wei Xu, Zhehui Wang, Jiansheng Hu, Rajesh Maingi, Carlos Romero-Talamas, and David M. Oschwald

Citation: Review of Scientific Instruments **89**, 10E112 (2018); doi: 10.1063/1.5036633
View online: https://doi.org/10.1063/1.5036633
View Table of Contents: http://aip.scitation.org/toc/rsi/89/10
Published by the American Institute of Physics

Initial results and designs of dual-filter and plenoptic imaging for high-temperature plasmas

Zhen Sun,[1] Jon K. Baldwin,[2] Wei Xu,[1] Zhehui Wang,[2,a)] Jiansheng Hu,[1] Rajesh Maingi,[3] Carlos Romero-Talamas,[4] and David M. Oschwald[2]
[1]*Institute Plasma Physics, Chinese Academy of Sciences, Hefei, AH 230031, China*
[2]*Los Alamos National Laboratory, Los Alamos, New Mexico 87545, USA*
[3]*Princeton Plasma Physics Laboratory, Princeton, New Jersey 08544, USA*
[4]*University of Maryland, Baltimore County, Maryland 21250, USA*

(Presented 18 April 2018; received 17 April 2018; accepted 29 August 2018; published online 4 October 2018)

Mass injection has found new applications in magnetic fusion including edge-localized-mode control. Better understanding of injected-mass-plasma interactions requires spatially and temporally resolved diagnostics that can characterize the dynamics of the mass interactions with plasmas. Fast imaging can be used to characterize the ionization dynamics such as the propagation of the ionization front, which moves at the thermal sound or higher speed, and mixing of the neutral atoms with the ambient plasma. Multi-wavelength spectral imaging is promising since different parts of the plasma give different spectral signatures. Here we describe a dual-spectral imaging technique based on a monochromatic camera sensor and filters with two passing optical wavelengths. The method is shown to improve image contrast, and it compares favorably with alternatives such as color cameras and methods using a filter wheel. Further improvements through relative filter area ratios and plenoptic imaging are possible. The initial results from EAST and plenoptic imaging are also included. *Published by AIP Publishing.*
https://doi.org/10.1063/1.5036633

I. INTRODUCTION

Transients such as edge-localized modes (ELMs) and disruptions are prominent issues for H-mode operations in ITER[1] and fusion tokamak reactors. Unmitigated ELM bursts in ITER and fusion power plant will dump energy exceeding the material limits and significantly shorten the lifetime of the plasma facing components (PFCs), divertor, and also produce a source of impurities in the plasma. The intensity of ELMs must therefore be controlled to tolerable levels in reactor-class fusion devices. Solutions to tame the major transients have to minimize damages to the reactor hardware and reduce the downtime in-between the events, if they cannot be avoided. ELM controls, including both ELM suppression and ELM pacing, have been motivated by multiple purposes as discussed below, in addition to minimizing the divertor and first wall erosion associated with the largest ELMs or Type I ELMs.

The details of ELM physics are quite complex. Well diagnosed experiments remain an essential part of ELM physics studies as well as technology development for ELM controls. Experimentally, several types of ELMs are known based on observations. The goals of ELM control are as follows:[2–4] (a) To trigger ELMs without compromising the H-mode confinement or reducing the pedestal height; (b) to trigger ELMs to prevent impurity accumulation in the plasma core (ELM-free operation may face the impurity accumulation problem); (c) to control the ELM amplitude to prevent excessive PFC and divertor erosion or impurity generation near the edge; and (d) to trigger or suppress ELMs with a precise timing. The natural ITER-like ELMs are expected to have a frequency of a few Hz. (e) To control the footprint of the ELM wetting in the divertor region. (f) ELM triggering needs to be compatible with steady-state operations. EAST has recently achieved H-mode operation longer than 100 s and is uniquely suited for ELM technology development and understanding of ELM physics for long pulse plasmas.

Fast imaging is a powerful non-invasive technique to study the ELM triggering process using a pellet and other mass injection techniques. High spatial and temporal resolution of ELM-triggering or suppression processes can provide good experimental constraints for predictive modeling. Meanwhile, spectroscopic imaging is usually limited to a single spectral line per camera. The filter-wheel method is not quite effective in real time since mechanical rotation complicates the imaging process, and the temporal evolution of ELMs, in the order of microseconds to tens of microseconds, can be much faster than mechanical rotation. Here we describe a dual-spectral method using a single camera for multi-spectral imaging, as an alternative to color-camera and filter-wheel approaches.[5] The idea extends an earlier one for correlated velocimetry using a pair of matched filters.[6]

The paper is organized as follows. We first discuss the pellet ablation physics and some recent EAST fast camera imaging results, which motivate the improvement of contrast in real-time pellet imaging. We then describe the contrast improvement through using a dual-filter or "filter pair" method and the filters selected for lithium pellets. The initial

Note: Paper published as part of the Proceedings of the 22nd Topical Conference on High-Temperature Plasma Diagnostics, San Diego, California, April 2018.
a)Author to whom correspondence should be addressed: zwang@lanl.gov.

successful laboratory tests and first data from EAST then follow, including the design studies for plenoptic imaging.

II. DESIGN CONSIDERATIONS

Lithium granules have been successfully used in EAST for ELM controls. A few movie frames from imaging a lithium pellet ablation in an EAST plasma are shown in Fig. 1. While in the first three frames [(a)–(c)], two distinct regions, one with a bright spherical core and another with an elongated shape, are clearly identifiable, the distinction is lost in the other three frames shown.

The spherical core corresponds to the neutral-atom dominated region near the pellet. The elongated region is occupied mostly by the low-temperature plasmas that contain singly, doubly, and up to fully ionized lithium and low-temperature electrons. The elongation is due to the conformity of the plasmas to the magnetic flux tubes. The loss of distinction between the regions is because the emission from the plasma eventually became brighter than from the neutrals. The camera used an array of monochromatic sensors that do not distinguish different visible wavelengths. On the other hand, it is highly desirable to observe both regions in order to develop predictive models for lithium pellet ablation and better controls of ELMs. The open questions include how does the ELMs behavior change with the pellet size and timing? How much mass is needed for ELM suppression?

A. Ablation temporal and spatial scales

We may consider the lithium pellet ablation process in plasma using the model described previously.[4,12] The ablation rate of the atoms dN_p/dt due to the plasma heat flux q_∞ is given by

$$\frac{dN_p}{dt} = \frac{f_s A_p q_\infty}{H_0}, \tag{1}$$

where $A_p = 4\pi r_p^2$ is the surface area for a pellet sphere with a radius r_p and H_0 is the amount of energy required for each atom ablation. The value of H_0 is 1.4-1.6 eV for lithium. The empirical factor $0 < f_s < 1$ accounts for the heat shielding.

The layered structure surrounding a spherical pellet includes a spherical neutral cloud layer next to the pellet surface, which is then surrounded by plasmas of increased degrees of ionization and temperature. Various previous models have estimated that the neutral cloud sphere has a radius in the range of r_n = 2-10 r_p. For a pellet of 0.5 mm, the neutral cloud size is 1–5 mm. The lateral dimension of the low-temperature lithium plasma is comparable to the lithium ionization mean free path, $\Lambda_i = C_s/n_e \langle \sigma_i v_e \rangle$, for the lithium atom sound speed C_s, electron density n_e, and ionization rate $\langle \sigma_i v_e \rangle$. The ionization rate for the $Li^0 \rightarrow Li^+$ process was fitted by a nonlinear formula $4.28 \times 10^{-6} T_e/(T_e^{1.73} + 300) + 6 \times 10^{-8}$ cm^3/s based on the ADAS data.[13] For the peak ionization rate of 2.5×10^{-7} cm^3/s ($T_e \sim 30$ eV) and $C_s = 2$ km/s (corresponding to the temperature of 1615 K), $\Lambda_i = 0.8$ mm for $n_e = 10^{13}$ cm^{-3}. Therefore, the elongated plasma filament is about the same size as the neutral cloud diameter $2r_n + \Lambda_i \sim 2r_n$. The filamentary structure is hypothesized to be the ionization front moving around the plasma torus with the ion sound speed $\sim 10C_s$ or about 20 km/s.

The relevant time scales are the neutral cloud growth time r_n/C_s = 0.5–2.5 μs, the time for the plasma filament to fill up the camera field of view, 10 μs, and the plasma filament circulation time around the torus $2\pi R_0/10C_s = 580$ μs for the EAST tokamak major radius $R_0 = 1.85$ m. They can be compared with the ELM growth time in the order of 100 μs.

B. Contrast and resolution

Image contrast (C) can be used to characterize how well different regions of an image may be distinguished from one another. Following the definition by Rose,[7,8] the image contrast C of region A to region B is given by

$$C = \frac{|I_A - I_B|}{I_B}, \tag{2}$$

where I_A and I_B are the image intensities of the two regions A and B, respectively. The contrast between the neutral region and the plasma surrounding in Fig. 1 is 1.4, 1.4, 0.4, 0, 0, and 0 for image frames A to F, respectively.

The dual-filter concept is to isolate the emission from different regions so that dark-noise-limited or optimal contrast can be achieved, i.e., $I_B \geq I_0$ with I_0 being equivalent to the dark field intensity of the camera that can not be further reduced. Due to the statistical nature of the photons and electrical noise, none of the intensities I_A, I_B, and I_0 is a fixed quantity. Each of them can have an average value of $\bar{I}_A$, $\bar{I}_B$, and $\bar{I}_0$, respectively, and a corresponding standard deviation parameter σ_A, σ_B, and σ_0. In the Gaussian noise spectrum, σ_0 is the Gaussian width. In the Poisson fluctuation spectra, σ_A and σ_B corresponds to $\sqrt{I_A}$ and $\sqrt{I_B}$. When the number of photons per pixel is large, a Poisson fluctuation distribution can be approximated by a corresponding Gaussian distribution.

The spatial and temporal resolutions are also source emission-intensity and exposure-time dependent in high-speed imaging. The diffraction limited spatial resolution (δx_d) is given by

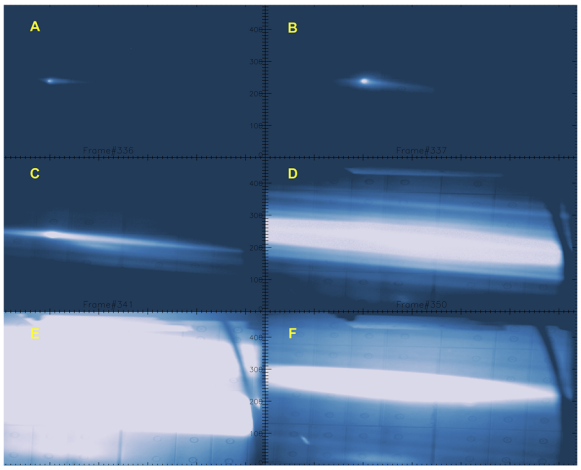

FIG. 1. An example of EAST lithium pellet ablation movie sequence starting from (a) to (f). Only in [(a)–(c)] we may separate the "neutral cloud" from the low-temperature "plasma cloud". More details are given in the text.

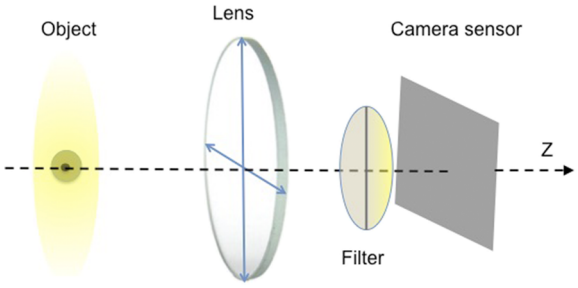

FIG. 2. The optics for the dual-filter implementation.

$$\delta x_d = 1.22\frac{f\lambda}{D}, \tag{3}$$

which in our case is about 14 μm (f = 0.5 m, D ~ 2 cm) and therefore smaller than the camera sensor pixel ($\delta x_p = 20$ μm). In other words, the diffraction limit poses a maximum aperture size D for any chosen f. The spatial resolution at the object location is therefore determined by

$$\delta x_o = \frac{n_p \delta x_p}{\mathcal{M}}, \tag{4}$$

with $\mathcal{M}$ being the magnification of the optics and $n_p \geq 2$ is an integer; i.e., we require that the minimum resolved length at the object location to be at least 2 pixels wide at the imaging position. The amount of light per pixel received is given by

$$I_p = T i_o(x, y) A \delta t, \tag{5}$$

where $0 < T < 1$ is the optical collection efficiency, $A = \delta x_o^2$ is the source area that contributes to the amount of light collected by the pixel, or "pixel intensity," δt is the integration time, and $i(x, y)$ is the source intensity per unit area and unit time. Here we have assumed that (a) the light emitting region is localized and therefore the integration along the line-of-sight is neglected for simplicity, and (b) the average intensity $i_o(x, y)$ is used for the time-integration window δt. The formula needs to be modified in high-speed imaging due to photon statistics.

Therefore, the light-limited spatial and temporal resolution for an individual pixel intensity I_p is given by

$$\frac{I_p}{\sqrt{I_p + I_0}} \geq k, \tag{6}$$

where k is typically chosen to be in the range of 3-5. For fixed exposure time δt, Eq. (6) determines the spatial resolution at the object location. For fixed spatial resolution, Eq. (6) determines the temporal resolution or the minimum exposure time needed. Either way, improving the contrast can also improve the resolution.

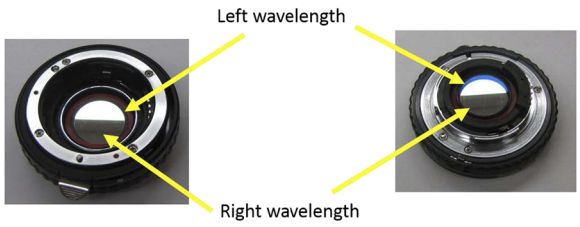

FIG. 3. A dual-filter is mounted onto the tube-extender for a Nikon mount. Two semi-circles of filters each with a diameter of 30 mm are glued together to form a full filter.

FIG. 4. The filter is inserted in-between a Nikon lens and the camera sensor, when in use.

TABLE I. A list of dual filter pairs made for lithium pellets. The wavelengths listed are the center of the passing spectral bands with a bandwidth of 10 nm.

	Left wavelength (nm)	Right wavelength (nm)
Pair A	610.3 ± 5	548.5 ± 5
Pair B	548.5 ± 5	460.3 ± 5

C. Optics and filter pairs

The optics setup is shown in Fig. 2. This setup is based on commercial optics (Nikon lenses) and Vision Research fast camera, both of which use a Nikon-mount. We design the dual filter based on the Nikon mount, as shown in Fig. 3. The installation is shown in Fig. 4.

Several dual filter pairs have been made and two of them are listed in Table I. The filters are for experiments using lithium pellets and powder or lithium conditioning discharges. Similar design can be implemented for other materials made of boron or other impurities.

III. RESULTS

A. Contrast studies using a laboratory plasma

The dual-filter design can be validated using different light sources such as a laser, LEDs, or a laboratory plasma. Here we used a laboratory RF magnetron plasma. The plasma was generated using 30 SCCM of argon flow into a vacuum chamber evacuated to 5.0×10^{-6} Torr base pressure and then maintained at a pressure of 10 mTorr. The RF frequency was at 13.56 MHz, and the power was fixed at 50 W. The argon gas flow was from the top of the chamber with the pressure being controlled by a throttle valve limiting the flow into the turbo-molecular pump.

The images from three different dual-filter surrogates are shown in the left of Fig. 5. Each of the surrogate consisted of a circular opening with a partially blocked area. The contrast improvement is shown more quantitatively through the line-out intensity comparison in the right column of Fig. 5. Vignetting needs to be considered for further analysis of the result; nevertheless, it gives us the basis to proceed with the dual-filter design.

B. EAST experiment

EAST is a premier magnetic fusion platform for plasma-material interaction, ELM control, and others.[9] Prior to the

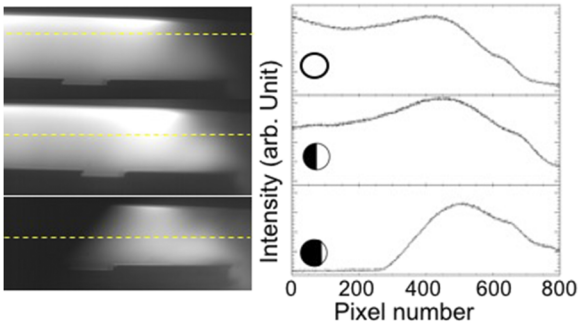

FIG. 5. Three circular inserts (see Fig. 4) with different blocked fractions were used to demonstrate the dual-filter concept through imaging a cm-size sputtering magnetic plasma source. Left column top to bottom, the fraction of an empty ring that is covered by a black tape increases from 0% to 50% and 75%. Right column, the line-out intensities from the images on the left column (dashed lines).

lithium injection measurements, two recent examples using the dual-filter pair are shown in Fig. 6 for lithium-coated wall discharges.

The good contrast between the left (Li I 460.3 ± 5 nm) and the right (Li II 548.5 ± 5 nm) is marked by the line separation near the middle (tilted toward right). A Vision Research Phantom 7.1 camera was used. The exposure time and sample rate were set at 41 ms and 24 frames/s, respectively. The H-mode plasma (EAST discharge #77758) for Fig. 6(a) has a plasma current I_p = 0.5 MA, upper single null (USN) configuration, and a line-averaged density $n_e = 3.5 \times 10^{19}$ m^{-3}. Auxiliary heating power included 1.0 MW lower hybrid wave (LHW) heating at 4.6 GHz, 0.5 MW LHW at 2.45 GHz, 1.6 MW neutral beam power, and 0.5 MW electron cyclotron resonance heating. The plasma (EAST discharge #77730) for Fig. 6(b) has a plasma current I_p of 0.4 MA, similar n_e with 2.0 MW LHW heating at 4.6 GHz, 1 MW LHW at 2.45 GHz, and 0.5 MW electron cyclotron resonance heating (ECRH).

Regions 1 and 2 in Fig. 6(a) correspond to Li I 460.3 ± 5 nm of Pair B in Table I. Region 3 corresponds to Li II. The bright region 2 indicates a possible intense plasma-wall interaction. The wall is coated with lithium. The thin strip at the bottom (region 4) indicates possible magnetization of the Li II with the emission aligned with local magnetic field line directions. A small piece of the black paper was added to the Li I side in Fig. 6(b), blocking the plasma

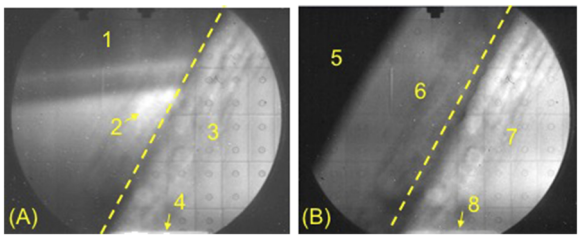

FIG. 6. Two examples of EAST plasma imaging using a dual-filter pair (Pair B in Table I). In both (a) and (b), the left side with respect to the dashed lines corresponds to the Li I neutral line filter centered at 460.3 ± 5 nm, and the right side corresponds to the Li^+ ion line filter centered at 548.5 ± 5 nm. More details are given in the text.

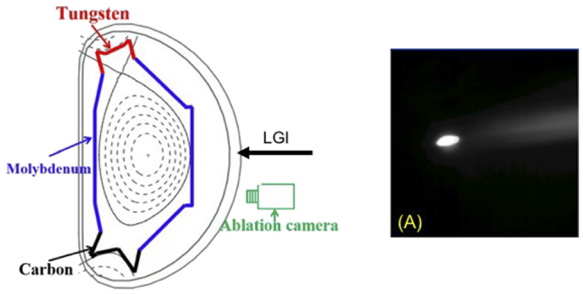

FIG. 7. (Left) Experimental setup to use the dual-filters for lithium pellet imaging in EAST. The ablation camera is modified with a dual-filter. (Right) A first image of lithium pellet inside a plasma using the dual-filter camera and a lithium granule injector (LGI).

emissions, as shown in region 5. Region 7 corresponds to region 3, and region 8 is similar to region 4. These results show that the dual filter design successfully separate different emission features, a necessary condition for lithium pellet imaging.

The use of a dual-filter for pellet imaging is illustrated in Fig. 7, where the filter was recently installed in the ablation camera and the first images obtained with the pellet experiment (EAST H-mode discharge #80852). In contrast with image frames in Fig. 1, the separation of the pellet region from ambient plasma cloud is demonstrated. Two unique features of the image are the removal of ablation cloud on one side of the pellet, and the shape of pellet core is clearly visible, which deviates from a sphere and indicates the effects due to the magnetic field.

C. Plenoptic imaging

Using a similar configuration to the setup, as shown in Fig. 2, we replace the dual-filter plane by a micro-lens array to form a light-field or plenoptic camera.[10,11]

We compare two Thorlab microlenslet arrays (MLA300-14AR-M and MLA150-7AR-M) for the initial designs. The key parameters are as follows: MLA300-14AR-M has a focal length f_m = 18.6 mm and a lenslet pitch D_m = 0.3 mm. MLA150-7AR-M has f_m = 6.7 mm and D_m = 0.15 mm. One of the known advantages of plenoptic imaging is refocusing

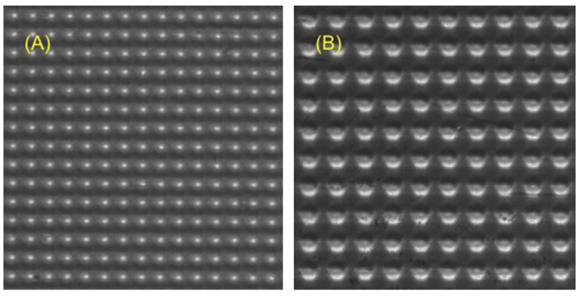

FIG. 8. Lenslet array to the camera sensor distance is chosen by forming a sharp image. (a) and (b) are images from the MLA150-7AR-M and MLA300-14AR-M microlenslet arrays, respectively. The spot sizes for (a) are smaller because of the smaller D_m, which is chosen for plenoptic demonstration.

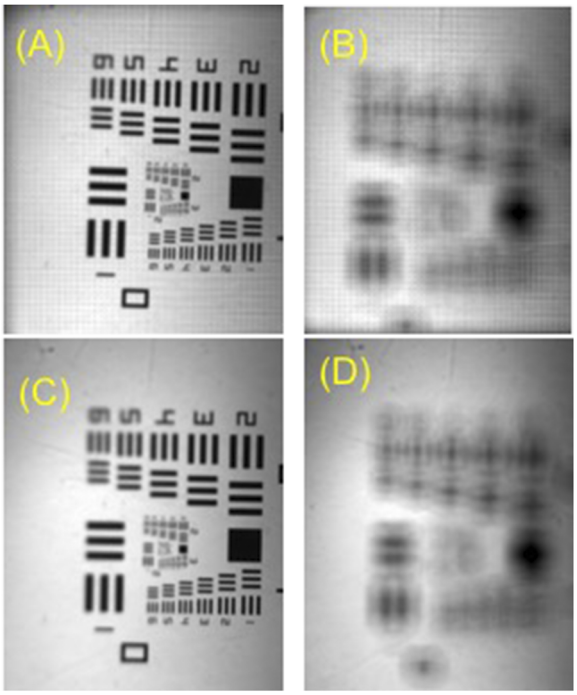

FIG. 9. (a) and (b), images of a 1951 USAF resolution test plate using the plenoptic setup. (a) is when a sharp image is formed, (b) is when the target is moved about 2.5 cm from the position in (a). (c) and (d) are corresponding images to (a) and (b) when the lenslet array is removed.

through computation or maximizing the aperture size without sacrificing the depth of field. It is important to position the camera sensor accurately at the focal plane of the microlenslets, i.e., the position accuracy needs to be within $\Delta x_p \cdot f_m/D_m$ for the pixel resolution Δx_p. For MLA300-14AR-M and Δx_p = 20 μm, the position accuracy is estimated to be 1.24 mm. For MLA150-7AR-M, the position accuracy is 0.89 mm for the same resolution. Sharp images are formed by scanning the relative distance between the lenslet array and the camera sensor plane, as shown in Fig. 8.

After the lenslet to the sensor distance is found, we add a normal lens (Nikon Nikkor 85 mm) in front of the lenslet (MLA150-7AR-M) and use a 1951 USAF resolution test plate for imaging. Several examples are included in Fig. 9 with and w/o the lenslet array. When the lenslet array is used, the normal image pattern is modulated by a periodic grid pattern generated by the lenslet array, as shown in Figs. 9(a) and 9(b). Further analysis of the data from the plenoptic camera prototype is underway.

In summary, we have designed and built several dual-filter sets to improve imaging contrast for lithium pellet experiments. A prototype plenoptic imaging system is also described and built. The first images of lithium pellets using the dual-filter enhanced camera have been successfully obtained. Similar concepts can also be applied to spectrally resolve high-speed imaging for other impurities in fusion plasmas and elsewhere. Further improvements through area-ratio optimization and plenoptic imaging are possible. The LANL work is supported in part by the US DoE/Fusion Energy Sciences Long Pulse Tokamak program.

[1]R. Aymar *et al.*, Plasma Phys. Controlled Fusion **44**, 519 (2002).
[2]Z. Wang *et al.*, "Physics of dust in magnetic fusion devices," in *New Aspects of Plasma Physics* (World Scientific, 2007), pp. 394–475.
[3]R. Maingi, S. J. Zinkle, M. S. Foster *et al.* US DoE/FES report on Plasma Materials Interactions, 2015.
[4]Z. Wang, R. Lunsford, D. K. Mansfield, and J. H. Nichols, J. Plasma Phys. **82**, 615820202 (2016).
[5]A web search using the key words "planetary imaging" can lead to a wealth of information and insights.
[6]Z. Wang, S.-N. Luo, C. W. Barnes, M. E. Briggs, D. L. Paisley, and S. F. Paul, Rev. Sci. Instrum. **77**, 10E516 (2006).
[7]A. Rose, *Vision, Human and Electronic* (Plenum Press, 1974).
[8]A. E. Burgess, J. Opt. Soc. Am. A **16**(3), 633 (1999).
[9]Z. Sun *et al.*, IEEE Trans. Plasma Sci. **46**(5), 1076 (2018).
[10]E. H. Adelson and J. Y. A. Wang, IEEE Trans. Pattern Anal. Mach. Intell. **14**(2), 99 (1992).
[11]R. Ng, M. Levoy, M. Brédif *et al.*, Technical Report CSTR 2005-02, Stanford University Computer Science, 2005.
[12]Z. Wang and G. A. Wurden, Rev. Sci. Instrum. **74**, 1887 (2003).
[13]Y. M. Wang, X. Q. Xu *et al.*, "Non-linear simulations of the ELM triggering by the deuterium/hydrogen pellet injection in a divertor geometry using the BOUT$_{++}$ code," Nucl. Fusion (submitted).